Somatostatin interneurons restrict cell recruitment to retinally driven spontaneous activity in the developing cortex

Leighton, Alexandra H; Cheyne, Juliette E; Houwen, Gerrit J; Maldonado, Paloma P; De Winter, Fred; Levelt, Christiaan N; Lohmann, Christian

published in
Cell Reports
2021

DOI (link to publisher)
10.1016/j.celrep.2021.109316

document version
Publisher's PDF, also known as Version of record

Cell Reports

Somatostatin interneurons restrict cell recruitment to retinally driven spontaneous activity in the developing cortex

Graphical abstract

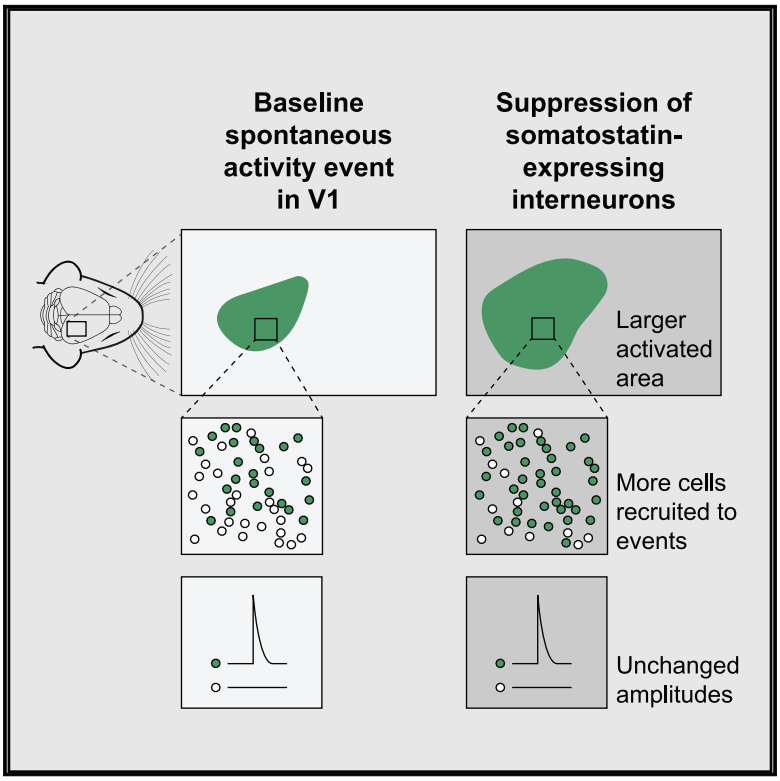

Authors

Alexandra H. Leighton, Juliette E. Cheyne, Gerrit J. Houwen, Paloma P. Maldonado, Fred De Winter, Christiaan N. Levelt, Christian Lohmann

Correspondence

c.lohmann@nin.knaw.nl

In brief

To refine developing connections, the neonatal visual cortex relies on spontaneous activity patterns, low (L-) and high (H-) synchronicity events, with precise spatiotemporal characteristics. Leighton et al. demonstrate that somatostatin (SST)-expressing interneurons control these characteristics by restricting the cell number and cortical area activated by retinally driven events.

Highlights

- Spontaneous retinal “L-events” activate small areas of neonatal visual cortex
- Somatostatin interneurons restrict activation area and cell recruitment
- Retina-independent “H-events” activate larger areas of cortex than L-events
- H- and L- events are characterized by distinct excitatory/inhibitory input ratios

Leighton et al., 2021, Cell Reports *36*, 109316
July 6, 2021
https://doi.org/10.1016/j.celrep.2021.109316

Cell Reports

CellPress
OPEN ACCESS

Report

Somatostatin interneurons restrict cell recruitment to retinally driven spontaneous activity in the developing cortex

Alexandra H. Leighton,[1] Juliette E. Cheyne,[1,6] Gerrit J. Houwen,[1] Paloma P. Maldonado,[1] Fred De Winter,[2] Christiaan N. Levelt,[3,4] and Christian Lohmann[1,5,7,*]

[1]Department of Synapse and Network Development, Netherlands Institute for Neuroscience, 1105 BA Amsterdam, the Netherlands
[2]Department of Neuroregeneration, Netherlands Institute for Neuroscience, 1105 BA Amsterdam, the Netherlands
[3]Department of Molecular Visual Plasticity, Netherlands Institute for Neuroscience, 1105 BA Amsterdam, the Netherlands
[4]Department of Molecular and Cellular Neurobiology, Center for Neurogenomics and Cognitive Research, VU University Amsterdam, Amsterdam, the Netherlands
[5]Department of Functional Genomics, Center for Neurogenomics and Cognitive Research, VU University Amsterdam, Amsterdam, the Netherlands
[6]Present address: Physiology Department, Centre for Brain Research, University of Auckland, Auckland, New Zealand
[7]Lead contact
*Correspondence: c.lohmann@nin.knaw.nl
https://doi.org/10.1016/j.celrep.2021.109316

SUMMARY

During early development, before the eyes open, synaptic refinement of sensory networks depends on activity generated by developing neurons themselves. In the mouse visual system, retinal cells spontaneously depolarize and recruit downstream neurons to bursts of activity, where the number of recruited cells determines the resolution of synaptic retinotopic refinement. Here we show that during the second post-natal week in mouse visual cortex, somatostatin (SST)-expressing interneurons control the recruitment of cells to retinally driven spontaneous activity. Suppressing SST interneurons increases cell participation and allows events to spread farther along the cortex. During the same developmental period, a second type of high-participation, retina-independent event occurs. During these events, cells receive such large excitatory charge that inhibition is overwhelmed and large parts of the cortex participate in each burst. These results reveal a role of SST interneurons in restricting retinally driven activity in the visual cortex, which may contribute to the refinement of retinotopy.

INTRODUCTION

Newborns can interact with their environment and perform sensorimotor tasks soon after birth, without any previous experience of patterned sensory input. These abilities rely on extensive preparation by the developing nervous system before the onset of sensory experience. Initially, neuronal networks are roughly outlined by molecular guidance cues and subsequently refined by activity-dependent processes. During this refinement phase, spontaneously depolarizing cells in the sensory organs and the brain (Blankenship and Feller, 2010) initiate and propagate patterned "training" activity across the developing network, strengthening well-targeted synapses and weakening others.

In the mouse visual system, neonatal retinae generate bursts of activity that travel downstream and refine retinotopic maps, as well as the segregation of contralateral and ipsilateral afferents through Hebbian and non-Hebbian mechanisms (Kirkby et al., 2013). As a result of this fine-tuning, neurons in the mouse visual cortex can respond to visual information before the eyes open at post-natal day (P) 14 (Cang et al., 2005; Ko et al., 2013; Rochefort et al., 2011; Zhang et al., 2011).

Spontaneous activity patterns can be described and distinguished by burst characteristics, such as frequency, duration, synchronicity of firing between cells, lateral spread, and the number of cells that participate (Ackman and Crair, 2014; Albert et al., 2008; Allene and Cossart, 2010; Colonnese and Phillips, 2018; Kerschensteiner, 2014; Luhmann and Khazipov, 2018). A growing body of work has shown that merely the presence of activity is not sufficient for refinement, but that these specific activity characteristics encode and transmit essential information required by the brain to develop normally (Kirkby et al., 2013; Leighton and Lohmann, 2016). The number of cells activated by each burst may determine the resolution with which spontaneous activity can refine connections between cells; for instance, if retinal waves recruit too many neurons, retinotopic map refinement is prevented (Burbridge et al., 2014; Xu et al., 2011, 2015). In contrast, eye-specific segregation can be impaired by changes in burst frequency (Burbridge et al., 2014; Xu et al., 2011).

Two types of spontaneous activity are found in the primary visual cortex (V1): retinally driven, low-synchronicity events with low cell participation rates ("L-events"; Ackman et al., 2014;

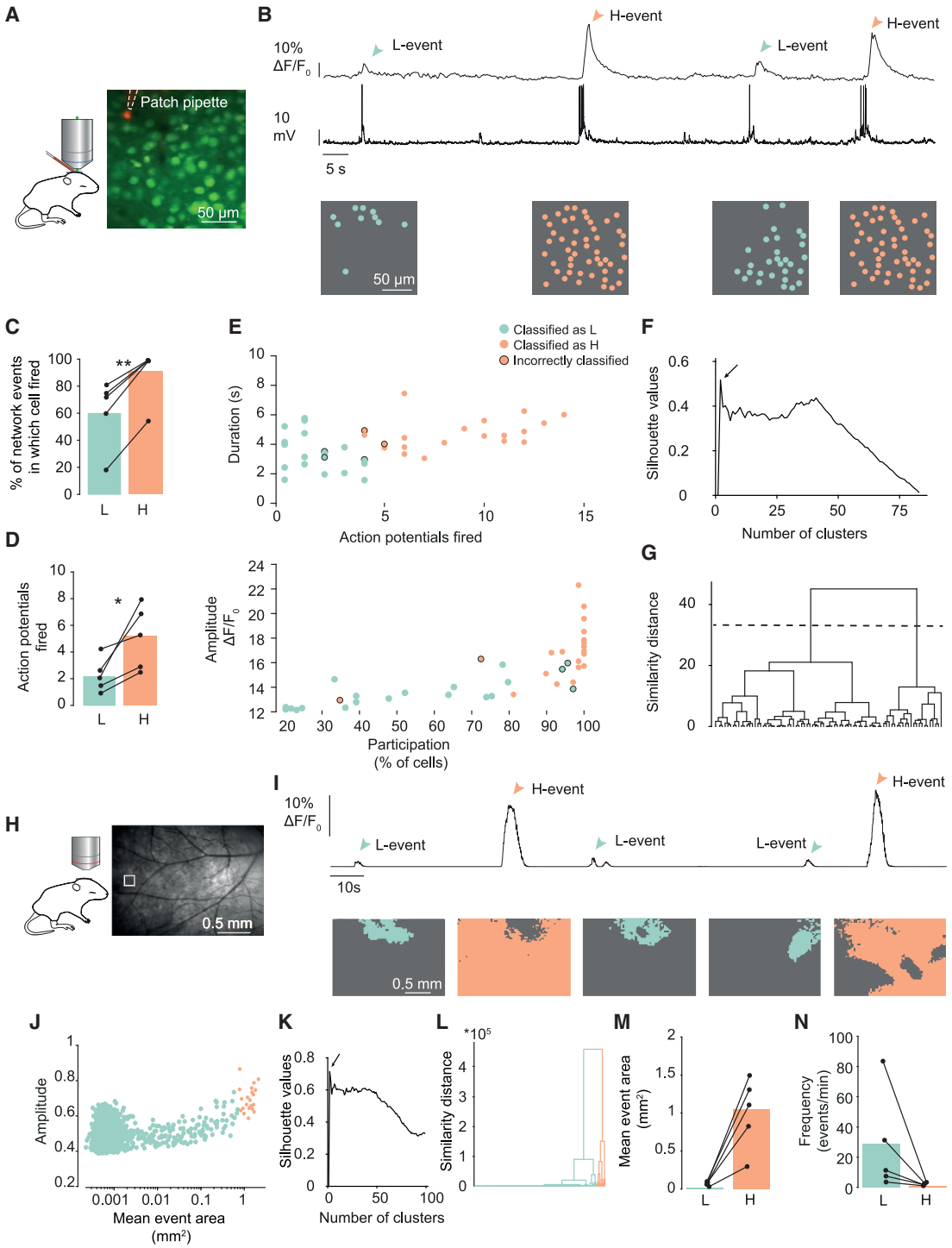

Figure 1. Distinct spontaneous activity patterns occur in the visual cortex during the second post-natal week

(A) Cells in V1 L2/3 were loaded with the calcium indicator Oregon Green Bapta 1-AM (green) to track spontaneous activity patterns. The recorded cell was filled with Alexa 594 via the patch pipette for identification (red).

(B) L-events (blue arrowheads) and H-events (orange arrowheads) shown as a calcium trace (average activity of all imaged cells) with simultaneous whole-cell current-clamp recording. The cells that participated in each event are displayed as filled circles below.

(C) Cells fired action potentials during a higher percentage of H-events than L-events ($p = 0.001$, paired t test; $n = 5$ cells).

(D) More action potentials were fired during H-events than during L-events ($p = 0.03$, paired t test; $n = 5$ cells).

(legend continued on next page)

Gribizis et al., 2019; Siegel et al., 2012) and retina-independent, high-synchronicity events with high cell participation and amplitude ("H-events"; Gribizis et al., 2019; Hanganu et al., 2006; Siegel et al., 2012). It is possible that these different types of events work together to pattern the developing cortex, where sparse activation and retinal origin of L-events gives them the resolution required to shape the network according to the organization of the eye, whereas global events (H-events) could allow neurons to perform synaptic homeostasis, bringing synaptic strengths back to a workable range (Siegel et al., 2012). Indeed, computational modeling of this joint organization leads to topographically refined receptive fields and sparsification of activity over time (Wosniack et al., 2021).

In adults, we have an increasing appreciation of the strong and specific regulation of network activity by interneuron subtypes (Kepecs and Fishell, 2014; Markram et al., 2004; Tremblay et al., 2016; van Versendaal and Levelt, 2016), but little is known about interneuron subtype activity in neonates. Recent work has shown that GABAergic cells exert an inhibitory effect on the cortical network as early as the start of the second post-natal week *in vivo* (Che et al., 2018; Kirmse et al., 2015; Minlebaev et al., 2007; Valeeva et al., 2016), and that they are active in assemblies (Duan et al., 2020; Modol et al., 2020). GABAergic cells can regulate cortical activity patterns (Duan et al., 2020), and modeling the blocking of GABAergic transmission increased spontaneous activity cluster size (Rahmati et al., 2017). During the same developmental window, somatostatin (SST)-expressing interneurons form strong synapses onto pyramidal cells, weakening to adult levels upon eye opening (Guan et al., 2017). In the adult brain, SST interneurons can control the size of memory engrams in the adult hippocampus (Stefanelli et al., 2016) and exert lateral inhibitory control in the auditory (Kato et al., 2017) and visual cortex (Adesnik et al., 2012). We therefore investigated here whether the strong inhibition mediated by SST interneurons before eye opening also restricts cell recruitment and event size during spontaneous activity.

RESULTS

L-events recruit fewer cells and show restricted lateral spread

L- and H-events were previously described using two-photon calcium imaging of populations of around 50 cell somas (Siegel et al., 2012). To understand how L- and H-characteristics match up to other reports of spontaneous activity, we measured their properties at a range of different scales. First, we used whole-cell current-clamp recordings to compare cell recruitment between L- and H-events in V1 layer 2/3 neurons *in vivo*, in lightly anesthetized (0.7%–1% isoflurane) mouse pups between P8 and P12 (Figure 1A). Simultaneous two-photon calcium imaging (using Oregon Green Bapta 1-AM) allowed identification of L- and H-events (Figure 1B), where events with over 80% participation were considered H-events (Siegel et al., 2012). We confirmed that L-events have lower cell participation, because patched cells almost always fired during H-events, but not during L-events (Figure 1C). Neurons also fired significantly more action potentials during H-events than during L-events, in correspondence with their higher calcium transient amplitude (Figure 1D). L-event duration (mean 4.6 s) was similar to the duration of retinal waves (summarized in Torborg and Feller, 2005), in line with their largely retinal origin.

To confirm our previous split of these events into two distinct groups (L and H) in a manner independent of calcium imaging, we performed hierarchical clustering using the number of action potentials fired and the duration of bursts (Figure 1E). Silhouette analysis revealed an optimum of two clusters (Figure 1F). This split (Figure 1G) corresponded well (76% overlap) to our original definition of L- and H-events, where events with between 20% and 80% participation were classified as L-events, and those over 80% network participation were identified as H-events (Siegel et al., 2012). We therefore continued to use this 80% cutoff to distinguish L- and H-events during two-photon network calcium imaging.

When using two-photon microscopy, H-events activated almost all neurons in the field of view. To measure lateral spread of events, we used *in utero* electroporation to widely express GCaMP6s, allowing us to record a much larger part of the visual cortex (4.9 mm^2) with wide-field imaging (Figure 1H). At this large population level, two types of events were still clearly detectable (Figure 1I). Silhouette analysis again revealed an optimal separation at two clusters (Figures 1J and 1K), splitting the data into events occurring locally and with low amplitudes (local events) and events with large spatial spread and with high amplitudes (Figures 1L and 1M), presumably corresponding to L- and H-events. Over the whole field of view, L-events occurred at higher frequencies than H-events (Figure 1N). To compare these measurements with the frequencies obtained with two-photon calcium imaging, we also measured event frequency at an area corresponding to the size of the field of view of our two-photon microscope. We found that widespread, putative H-events occurred at a frequency of 0.6 ± 0.25 events/min in this smaller area, similar to the previously determined frequency in two-photon experiments (0.5 per minute; Siegel et al., 2012). For local L-events, we saw an average of 0.37 ± 0.12 events/min in

(E) Action potentials from a single cell, labeled by outcome of hierarchical clustering. Outlined events were classified differently when the 80% participation criterion was used.
(F) Silhouette analysis of hierarchical clustering using burst duration and action potentials fired.
(G) Dendrogram of hierarchical clustering results for an example animal.
(H) Epifluorescence imaging of the visual cortex expressing GCaMP6s was used to image a larger field of view. White square indicates field of view in two-photon.
(I) Mean calcium responses during L- and H-events (top) and area of activation (bottom).
(J) Event amplitude by mean event area for all events detected in wide-field in an example animal, labeled according to classification by clustering.
(K) Silhouette analysis of hierarchical clustering using amplitude and event size as parameters.
(L) Dendrogram of hierarchical clustering results for an example animal.
(M) Mean event areas of wide-field L- and H-events.
(N) Frequency of each event type in activations per minute.

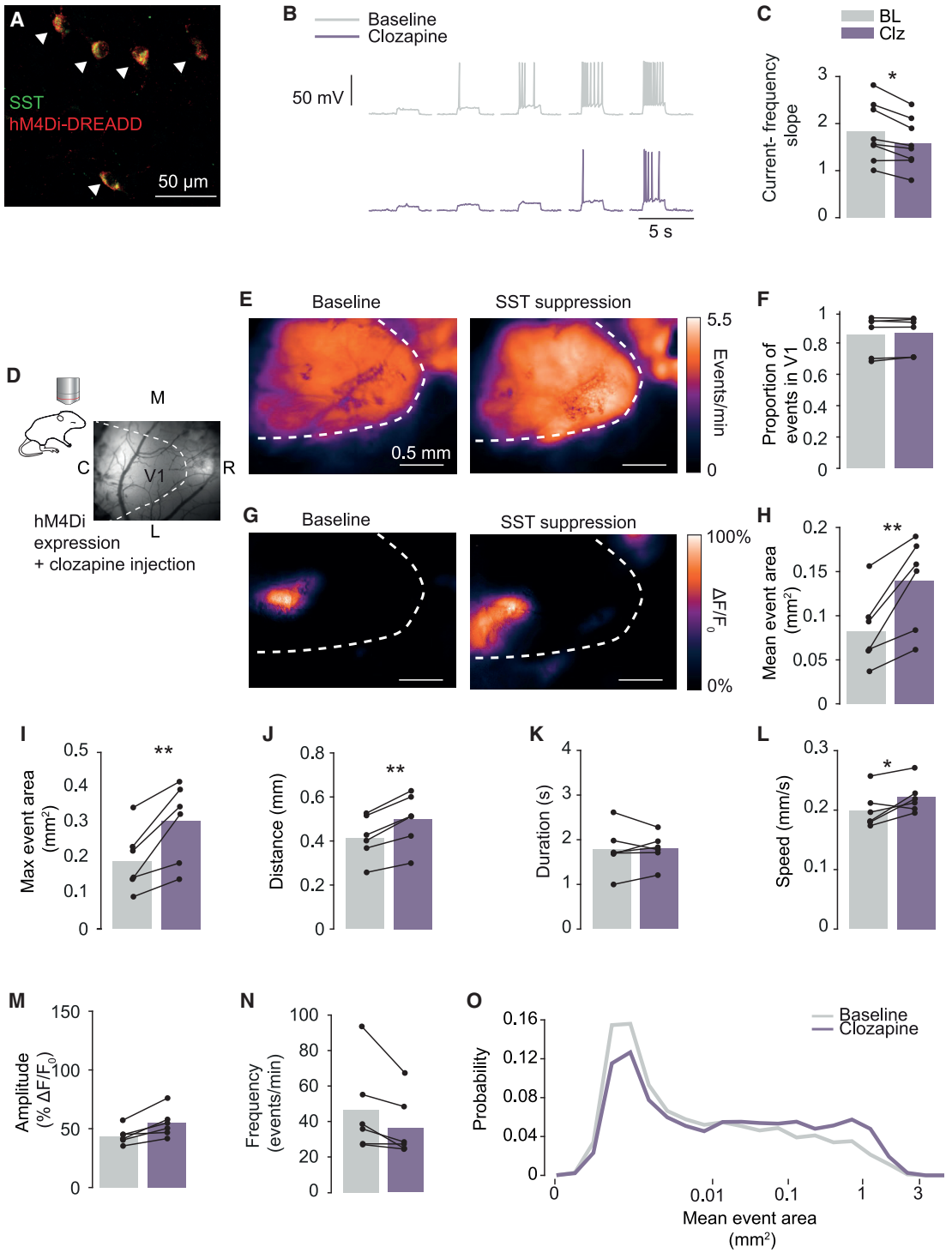

Figure 2. SST interneuron suppression selectively leads to larger event spread

(A) Section of the visual cortex of a P9 SST-cre mouse injected with AAV-hSyn-DIO-hM4D(Gi)-mCherry (red) with immunostaining for SST (green). All cells in the field of view were double labeled.

(B) Example cell firing at 30, 40, 50, and 60 pA injection before and after clozapine application.

(C) Clozapine application *in vitro* significantly reduced excitability in SST interneurons expressing the hM4Di-DREADD construct (n = 8 cells; paired t test, $p < 0.05$).

(legend continued on next page)

wide-field recordings, a lower frequency than the two-photon microscopy data (around 1 per minute) and in line with the reduced sensitivity of wide-field imaging to small, sparse activations of a few cells.

Taken together, L-events are characterized by low cell recruitment and local activation, as well as a low number of action potentials fired. In contrast, during H-events, large areas of the cortex are activated as a high density of cells fire in a burst of action potentials.

SST interneurons restrict spatial spread of spontaneous events

Given that in adulthood, SST interneurons control the size of memory engrams in the hippocampus (Stefanelli et al., 2016), as well as lateral inhibition in the auditory (Kato et al., 2017) and visual cortex (Adesnik et al., 2012), we asked whether SST interneurons also control the lateral spread of spontaneous activity during cortical development.

We selectively suppressed SST interneurons using a cre-dependent viral vector driving expression of an inhibitory hM4Di-DREADD (AAV-hSyn-DIO-hM4D(Gi)-mCherry) during calcium imaging of spontaneous activity in awake pups. 83% ± 8% of cells expressing the inhibitory hM4Di-DREADD also expressed SST (n = 4 animals; Figure 2A), and 79% ± 6% of SST interneurons expressed the hM4Di-DREADD. Activation of the hM4Di-DREADD with its fast-acting agonist clozapine reduced excitability of DREADD-expressing cells *in vitro* (Figures 2B and 2C) similar to the excitability-reducing effect of hM4Di-DREADD activation in developing layer 2/3 pyramidal neurons described previously (Naskar et al., 2019).

By co-injecting the hM4Di-DREADD vector with pAAV-Syn-GCaMP6s, network activity was recorded in awake pups across a large part of the cortex with wide-field imaging (field of view: 4.9 mm^2; Figure 2D), before and after subcutaneous clozapine (0.5 mg/kg) injection. To control for possible hM4Di-DREADD-independent effects of clozapine, results from a t test are reported as significant only when a linear mixed-effects model with an interaction term (of injected virus type and clozapine administration) demonstrated a significantly better fit than one without the interaction term.

We first quantified activity origin and spread of all events (Figure 2E). Although all events are included in the figure, L-events strongly dominate the observed activity pattern because they are much more frequent than H-events. Both before and after SST interneuron suppression, most activity originating in V1 was confined to this area (Figure 2F), indicating that much of the observed spontaneous activity was restrained by V1 boundaries independently of SST interneuron signaling.

Upon SST interneuron suppression, network events activated a significantly larger area of V1 (Figures 2G and 2H). This was due to both an increase in the maximum lateral spread (Figure 2I) and the distance traveled during each event (Figure 2J). We detected no difference in the duration of events (Figure 2K), but their speed of propagation across the cortex increased (Figure 2L) and allowed them to travel farther. We found no significant changes upon clozapine administration to control animals (Figure S1).

The increase in event area could be because of an increase in the relative frequency of H-events, or increased recruitment of cells to each spontaneous event. Given that the event amplitude did not show a significant change (Figure 2M), and that the frequency of activity showed a trend to decrease (Figure 2N), it seems more likely that each spontaneous event recruits more active cells upon SST interneuron suppression. Event size before and after SST interneuron suppression shows a shift away from small events and toward larger events (Figure 2O).

SST interneurons restrict cell recruitment to L-events

We repeated measurements of spontaneous activity during suppression of SST interneuron activity, using two-photon imaging (Figure 3A), again with co-injection of the hM4Di-DREADD vector with pAAV-Syn-GCaMP6s, or the pAAV-Syn-GCaMP6s vector alone in control animals. In control animals, clozapine injection did not significantly increase the frequency in any participation bin (Figures S2A and S2B). Upon SST interneuron suppression, the frequency of events in low-participation bins did not change (Figures 3B–3D). In contrast, suppressing SST interneurons specifically increased the frequency of events in the highest participation bin (Figure 3D). In this highest participation bin, a significant interaction effect was found between the expressed

(D) Wide-field imaging was used to record large-scale activity patterns in animals expressing GCaMP6s and an hM4Di construct in SST interneurons. SST interneurons were suppressed with clozapine (Clz) injection.
(E) Average activity frequency per pixel before (left) and after (right) clozapine injection to induce suppression of SST interneurons. Events were included only if they activated pixels within the V1 boundaries, but the entire field of view was used to measure event properties.
(F) There was no significant change in the proportion of events that activated V1 upon clozapine injection to induce suppression of SST interneurons (n.s., paired t test; n = 6 animals).
(G) Example event before (left) and after (right) suppression of SST interneurons.
(H) The mean area activated by each event increased upon suppression of SST interneurons (p = 0.006, paired t test; n = 6 animals).
(I) The max event area (the activated area during the largest frame of an event) was significantly higher after suppression of SST interneurons (p = 0.006, paired t test; n = 6 animals).
(J) Events traveled farther across the cortex after suppression of SST interneurons through clozapine injection (p = 0.00066, paired t test; n = 6 animals).
(K) After suppression of SST interneurons, the duration of events did not change (n.s., one-way ANOVA comparing linear mixed-effects model with and without an interaction term; n.s., interaction of injected genotype and clozapine injection; n = 6 animals).
(L) The speed of events increased after suppression of SST interneurons (p = 0.049, paired t test; n = 6 animals).
(M) No significant change in amplitude was detected after suppression of SST interneurons (one-way ANOVA comparing linear mixed-effects model with and without an interaction term; n.s., interaction of injected genotype and clozapine injection).
(N) The frequency of events did not change upon suppression of SST interneurons (n.s., paired t test; n = 6 animals).
(O) Distribution of mean area (over all active frames) of events before and after clozapine.
C, caudal; L, lateral; M, medial; max, maximum; n.s., not significant; R, rostral.

viral construct (1:1 hM4Di-DREADD with GCaMP6s compared with 1:1 diluted GCaMP6s) and clozapine injection (two-way ANOVA, interaction of clozapine and viral injection, $p = 0.0008$).

This observation could either mean that SST interneuron suppression allows more "true" H-events to occur in the network, or that SST interneuron suppression causes events to recruit more cells, increasing participation. Either explanation would increase the average area of events, as seen in the wide-field imaging (Figure 2H).

To distinguish between these scenarios, we assessed whether event amplitude (a proxy for the number of action potentials fired) increased upon SST interneuron suppression, because true H-events are associated with large event amplitudes. We did not detect an increase in mean event amplitude of participating cells, either as a paired t test comparing baseline with clozapine administration or when taking the control experiments into account and testing for a significant interaction effect of injected construct and clozapine administration (Figure 3E; control in Figure S2B), supporting the idea that SST interneuron suppression increases recruitment to events. In this scenario, events that would normally fall short of our detection threshold of 20% participation may cross into our definition of an event, explaining why we detect this effect in only the highest participation bin.

Furthermore, careful analysis of neuronal participation and amplitude revealed that SST interneuron suppression specifically facilitated high participation events of low amplitude (Figures 3F and 3G; for controls, see Figure S2C), indicating increased recruitment of cells to L-events.

Because the wide-field imaging data did not show an increase in event amplitude or frequency (Figures 2M and 2N), it seems likely that the increase in frequency seen in two-photon imaging experiments reflected a larger proportion of events entering the field of view because of their lateral spread, rather than a true increase in the number of events. SST interneuron suppression therefore changes cell recruitment without affecting the firing rate of active neurons.

During baseline spontaneous activity, we did not detect a difference between the average participation of SST-expressing interneurons and the average participation of the rest of the cell population (Figure S3A); SST-expressing interneurons participated during both L- (Figure S3B) and H-events (Figure S3C). In addition, we did not detect a difference in amplitude during L- (Figure S3D) or H-events (Figure S3E).

Together, SST interneuron activity restricts the lateral spread and cell activation density of local L-events, but not their frequency or the overall firing rates of individual neurons during network events.

Excitatory and inhibitory balance during L- and H-events

Our observation that reducing SST interneuron-mediated inhibition affected the spread of L-events, without converting them (in terms of action potential firing frequency) into H-events, suggested that the difference between these two types of event was not caused simply by reduced recruitment of inhibition. More likely, differences in excitatory drive underlie the difference between L- and H-events, where SST interneurons participate in both events but are overwhelmed by excitation during H-events. To test this directly, we recorded synaptic inputs received by the soma during L- and H-events in lightly anesthetized pups. We performed *in vivo* whole-cell recordings in voltage-clamp mode, while simultaneous calcium imaging of the network allowed identification of L- and H-events. As reported previously, events involved both glutamatergic and GABAergic synapses (Figure 4A; Colonnese, 2014; Hanganu et al., 2006; Minlebaev et al., 2007). In line with the higher network participation in H-events, both the excitatory and inhibitory charge transferred (defined as area under the curve of the synaptic currents during a burst) were larger during H-events than during L-events (Figures 4B–4D). However, the ratio of excitatory charge transferred between H- and L-events was much larger than that of inhibitory charge transfer (Figure 4E). This confirms that H-events differ from L-events mainly because of a much stronger excitatory drive rather than to differences in inhibitory inputs.

To confirm directly that H- and L-events could be differentiated more reliably based on excitation or inhibition, we trained a random forest classifier (Breiman, 2001) using only electrophysiological measurements to decode whether an event was an L- or an H-event. Peak current amplitude, mean current amplitude, total charge transferred, and duration of either inhibitory or excitatory current inputs were provided to the classifier. Training event classification was based on the original definition of 20%–80% (L-events) and over 80% participation (H-events) in network events obtained with two-photon calcium imaging. For all animals, the classifier trained on the excitatory data performed significantly better than the classifier trained on the inhibitory data, as demonstrated by the larger area under the curve of the receiver-operator characteristics (ROC) curve (Figures 4F and 4G). We conclude that differences in excitatory drive underlie the main characteristics of H- and L-events, while SST interneuron-mediated inhibition exerts much stronger control over L- than over H-events.

DISCUSSION

SST interneurons are crucial for activity-dependent maturation throughout the development of the nervous system. In the hippocampus and entorhinal cortex, long-range SST-expressing "hub" cells synchronize spontaneous activity (Bonifazi et al., 2009; Mòdol et al., 2017), and activating SST interneurons can trigger synchronous network depolarizations in slices (Flossmann et al., 2019). In the cortex, SST interneurons appear to be precocious (Pan et al., 2019), maturing before fast-spiking interneurons and even supporting the integration of fast-spiking interneurons into the network. SST interneurons in deep cortical layers receive dense but transient innervation from thalamocortical inputs during the first post-natal week (Marques-Smith et al., 2016; Tuncdemir et al., 2016), which facilitates the thalamocortical innervation of parvalbumin (PV)-expressing interneurons (Tuncdemir et al., 2016).

In cortical L2/3, SST interneuron synapses onto pyramidal cells emerge at the beginning of the second post-natal week (Guan et al., 2017), when oxytocin release also increases SST interneuron excitability and sparsifies neuronal activity (Maldonado et al., 2021). At this age, SST interneuron-mediated inhibition is strong and can be readily recorded in the somas of cortical pyramidal neurons. After eye opening, the strength of the

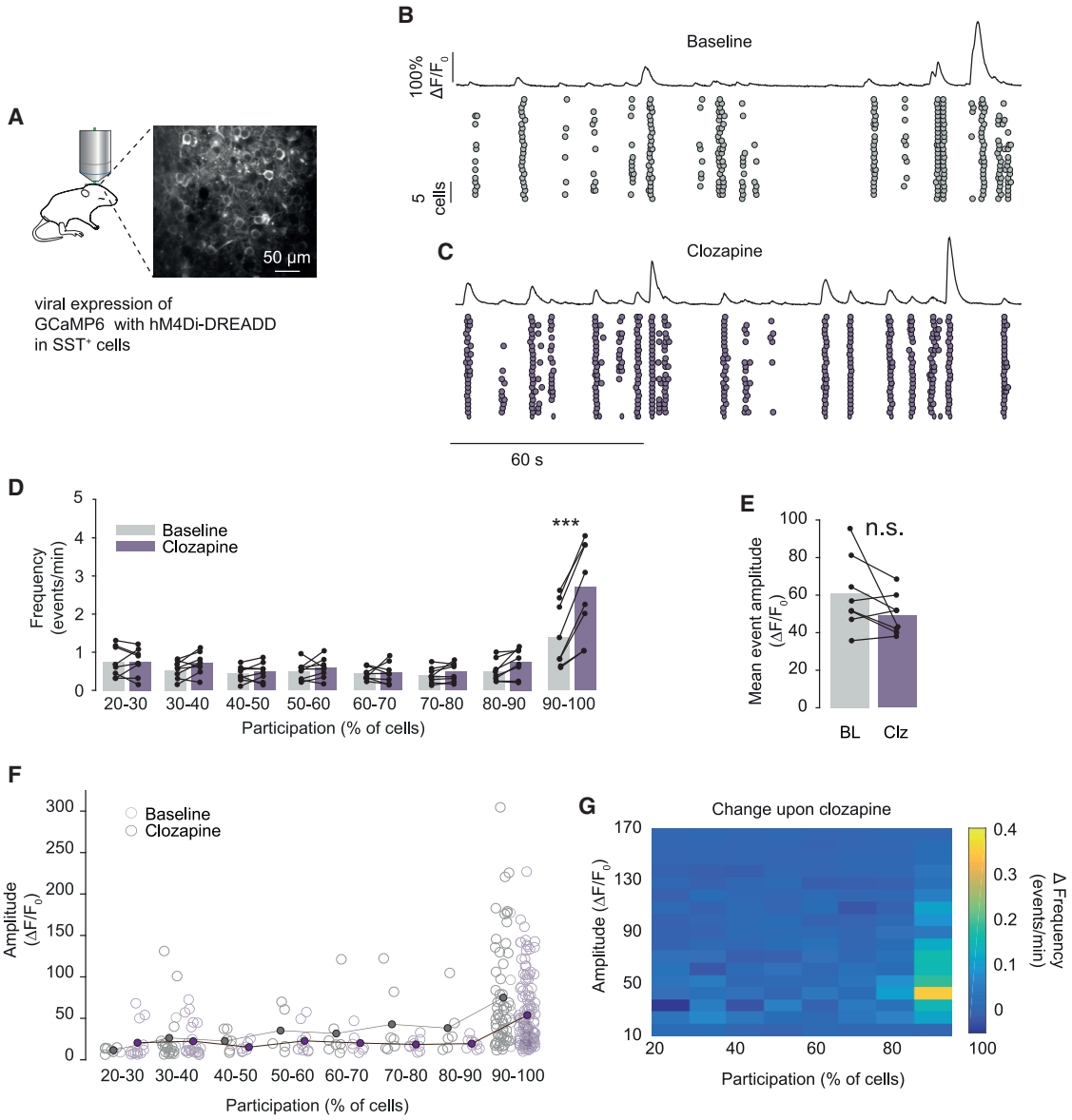

Figure 3. Suppressing SST interneuron activity selectively increases the number of high-participation low-amplitude events

(A) Two-photon imaging was used to record calcium transients in animals expressing GCaMP6s and an inhibitory hM4Di-DREADD construct in SST interneurons. Clozapine was injected at low concentrations to activate the hM4Di-DREADD and reduce SST interneuron excitability.

(B) Neurons were imaged in awake pups during the second post-natal week. Example recording before injection of clozapine. Shown is the average network activity of all cells in the field of view (top) and when each cell participated in an event (bottom). Each circle represents a calcium transient in a cell.

(C) Example recording after SST interneuron suppression. Shown is the average network activity of all imaged cells (top) and the activity of each imaged cell (bottom). Each circle represents a calcium transient in a cell.

(D) After SST interneuron suppression, there is a significant increase in the frequency of events only in the highest participation bin ($p = 0.0002$, threshold for significance at 0.0063 after Bonferroni correction for 8 comparisons, paired t test; n = 8 animals). Number of 90%–100% participation events, baseline condition: 261, clozapine condition: 607.

(E) No change in amplitude was detected upon suppression of SST interneurons (n.s., paired t test; n = 8 animals). Amplitude is measured as the average peak amplitude of all cells that participate in the event.

(F) Amplitude and participation of each event before and after clozapine in an example animal expressing hM4Di-DREADD.

(G) Heatmap showing the change in frequency of activity in events/min after suppression of SST interneurons. The largest increase occurred in high-participation/low-amplitude events.

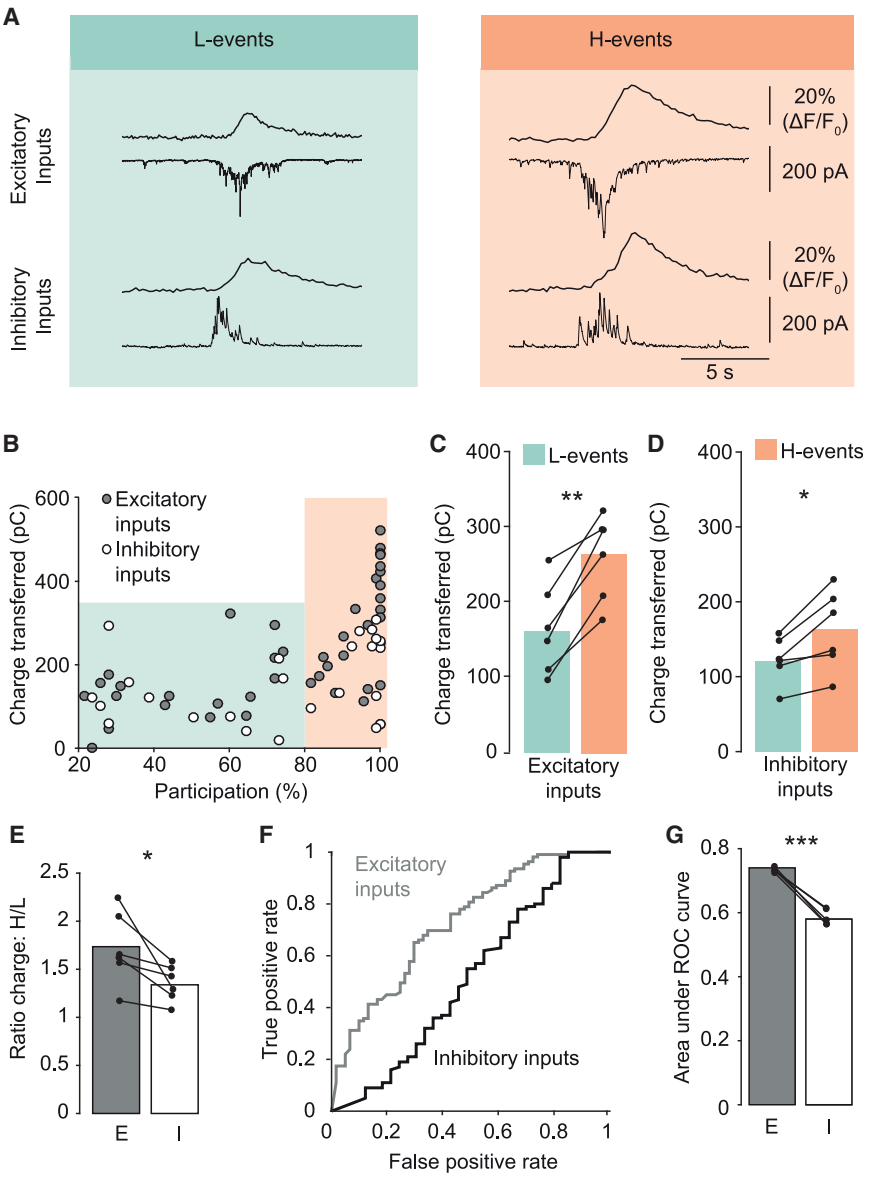

Figure 4. Excitatory and inhibitory synaptic inputs during L- and H-events

(A) *In vivo* voltage-clamp recordings combined with network calcium imaging in layer 2/3 V1 neurons. Excitatory and inhibitory inputs were measured alternatingly by switching the holding potential to the reversal potential of inhibitory or excitatory currents, respectively. Four events in an example cell, showing inhibitory and excitatory inputs received by the cell during an L-event and an H-event. Average calcium traces are shown from all imaged cells (top). Current traces (bottom) represent synaptic inputs onto the recorded neuron.

(B) Absolute transferred charges of excitatory and inhibitory input currents during network events of different participations in one cell.

(C) The excitatory charge transferred was significantly higher during H-events than during L-events ($p = 0.001$, paired t test; $n = 6$ animals).

(D) The inhibitory charge transferred was significantly higher during H-events than during L-events ($p = 0.016$, paired t test; $n = 6$ animals).

(E) The H:L ratio of charge transferred was significantly larger for excitatory than for inhibitory inputs ($p = 0.036$, paired t test; $n = 6$ animals).

(F) Example receiver operating characteristics (ROC) curve for one animal, showing a random forest classifier trained on excitatory or inhibitory data. The larger area under the curve for excitatory inputs indicates a higher success rate of classifying L- and H-events correctly when excitatory data were used compared with inhibitory data.

(G) Quantification of the area under the ROC curve for all animals. The area under the curve is significantly higher for classifiers trained on excitatory input data than for those trained on inhibitory input data ($p = 0.0002$, paired t test; $n = 5$ animals).

synaptic connection from SST interneurons to pyramidal cells sharply decreases. So far, the role of this strong SST interneuron-mediated inhibition during the second post-natal week is unknown.

Here, we found that during this period, suppression of SST interneurons increased the number of cells recruited to L-events and widened their lateral spread. This is in line with the strong influence of SST synapses and the early functional maturation of SST interneurons. Furthermore, this observation extends previous findings that interneurons restrict correlated activity to neuronal assemblies in the somatosensory cortex during early cortical development (Duan et al., 2020; Modol et al., 2020). It also matches the function of SST interneurons in adult mice, where they have extensive axonal arbors in L1 (Urban-Ciecko and Barth, 2016) and exert control over large distances through lateral inhibition in the visual (Adesnik et al., 2012) and auditory (Kato et al., 2017) cortex. Accordingly, upon suppression of SST interneurons during adulthood, cell recruitment in hippocampal engrams increases (Stefanelli et al., 2016), as does network synchronicity (Chen et al., 2015). Under wide-field imaging, the largest events did not seem to increase their size, suggesting that H-events are less affected by the suppression of SST interneurons. However, specific pharmacological isolation of H-events would be necessary to understand whether SST interneuron suppression affects these events alongside L-events.

A large body of work has shown that the features of spontaneous activity patterns are instructive in wiring the developing brain (Feller, 1999; Katz and Shatz, 1996). Manipulations of the size or frequency of retinal waves have directly demonstrated the importance of accurate patterning of spontaneous activity for fine-tuning the ascending visual pathways (Burbridge et al., 2014; Xu et al., 2015). Using a wide range of techniques, we have described L-events as activity patterns during which relatively few cells are weakly activated. Because the spread of activity patterns constrains the degree of synaptic refinement, SST

interneurons may optimize early activity patterns for establishing precise neuronal connections during the second post-natal week. We hypothesize that the largely retinal origin (Siegel et al., 2012) and restricted size of L-events allows them to mediate refinement of the network, because their localized nature maintains topographic specificity.

In contrast with local L-events, H-events are highly synchronized in time and drive substantial areas of the cortex to fire large numbers of action potentials. The high spatial spread and temporal synchronicity of H-events make them less suitable to convey information about cell arrangement in the retina. Instead, H-events may perform synaptic homeostasis to maintain workable ranges of synaptic strength, perhaps in a similar mechanism as during slow-wave sleep (González-Rueda et al., 2018; Tononi and Cirelli, 2006). Indeed, Wosniack et al. (2021) recently modeled how Hebbian plasticity rules allow L-events to refine cortical topography, while H-events dynamically adapt their amplitude to keep synaptic strength in a workable range. We have previously shown that H- and L-events have distinct event characteristics, and that L-events and not H-events depend on retinal waves of activity. Here we find that in addition, H-events are also driven by much stronger excitatory influx than L-events, while inhibitory influx is only marginally larger. These observations may explain why suppression of SST interneurons did not turn L-events into H-events, because these events have similar inhibitory input strength, but different strength and sources of excitatory inputs. Most likely, the inhibitory inputs that can constrain the spread of L-events during their weaker excitatory influx are simply overwhelmed by the strong excitatory influx during H-events.

In conclusion, we find that SST interneurons exert robust inhibitory control over network activity during the second post-natal week, even though inhibitory signaling is not fully strengthened until after eye opening. It seems that not only do interneurons exert inhibitory control over this early age, but they shape activity patterns crucial for driving fine-tuning of the developing network. It remains to be understood how other interneuron subtypes shape spontaneous activity, and future experiments involving prolonged suppression of SST interneuron activity during the second post-natal week may reveal the consequences for receptive field properties in the adult visual cortex.

STAR★METHODS

Detailed methods are provided in the online version of this paper and include the following:

- KEY RESOURCES TABLE
- RESOURCE AVAILABILITY
  - Lead contact
  - Materials availability
  - Data and code availability
- EXPERIMENTAL MODEL AND SUBJECT DETAILS
  - Organism
  - Genotypes
- METHOD DETAILS
  - Surgeries
  - Calcium imaging methods
  - Image acquisition
  - Electrophysiology acquisition
- QUANTIFICATION AND STATISTICAL ANALYSIS
  - Image processing
  - Signal detection
  - Statistical tests

SUPPLEMENTAL INFORMATION

Supplemental information can be found online at https://doi.org/10.1016/j.celrep.2021.109316.

ACKNOWLEDGMENTS

The authors thank Cátia Silva, Alexander Heimel, and Julijana Gjorgjieva for their comments on this manuscript; Monique van Mourik for technical assistance; and Johan Winnubst and Guido Meijer for help with data analysis software. This work was supported by grants of the Netherlands Organization for Scientific Research (NWO, ALW Open Program grant no. 822.02.006 and ALWOP.216; ALW Vici grant no. 865.12.001) and the "Stichting Vrienden van het Herseninstituut."

AUTHOR CONTRIBUTIONS

Conceptualization: A.H.L., J.E.C., and C.L.; methodology: A.H.L., J.E.C., and G.J.H.; formal analysis: A.H.L., P.P.M., and J.E.C.; resources: F.D.W.; investigation: A.H.L., J.E.C., P.P.M., and G.J.H.; writing: A.H.L., C.N.L., and C.L.

DECLARATION OF INTERESTS

The authors declare no competing interests.

Received: November 3, 2020
Revised: April 11, 2021
Accepted: June 6, 2021
Published: July 6, 2021

REFERENCES

Aarts, E., Verhage, M., Veenvliet, J.V., Dolan, C.V., and van der Sluis, S. (2014). A solution to dependency: using multilevel analysis to accommodate nested data. Nat. Neurosci. *17*, 491–496.

Ackman, J.B., and Crair, M.C. (2014). Role of emergent neural activity in visual map development. Curr. Opin. Neurobiol. *24*, 166–175.

Ackman, J.B., Zeng, H., and Crair, M.C. (2014). Structured dynamics of neural activity across developing neocortex. BioRxiv. https://doi.org/10.1101/012237.

Adesnik, H., Bruns, W., Taniguchi, H., Huang, Z.J., and Scanziani, M. (2012). A neural circuit for spatial summation in visual cortex. Nature *490*, 226–231.

Albert, M.V., Schnabel, A., and Field, D.J. (2008). Innate visual learning through spontaneous activity patterns. PLoS Comput. Biol. *4*, e1000137.

Allene, C., and Cossart, R. (2010). Early NMDA receptor-driven waves of activity in the developing neocortex: physiological or pathological network oscillations? J. Physiol. *588*, 83–91.

Bates, D., Mächler, M., Bolker, B., and Walker, S. (2014). Fitting Linear Mixed-Effects Models using lme4. ArXiv, 1406.5823. https://arxiv.org/abs/1406.5823.

Blankenship, A.G., and Feller, M.B. (2010). Mechanisms underlying spontaneous patterned activity in developing neural circuits. Nat. Rev. Neurosci. *11*, 18–29.

Bonifazi, P., Goldin, M., Picardo, M.A., Jorquera, I., Cattani, A., Bianconi, G., Represa, A., Ben-Ari, Y., and Cossart, R. (2009). GABAergic hub neurons orchestrate synchrony in developing hippocampal networks. Science *326*, 1419–1424.

Breiman, L. (2001). Random Forests. Mach. Learn. *45*, 5–32.

Burbridge, T.J., Xu, H.-P., Ackman, J.B., Ge, X., Zhang, Y., Ye, M.-J., Zhou, Z.J., Xu, J., Contractor, A., and Crair, M.C. (2014). Visual circuit development requires patterned activity mediated by retinal acetylcholine receptors. Neuron *84*, 1049–1064.

Cang, J., Rentería, R.C., Kaneko, M., Liu, X., Copenhagen, D.R., and Stryker, M.P. (2005). Development of precise maps in visual cortex requires patterned spontaneous activity in the retina. Neuron *48*, 797–809.

Che, A., Babij, R., Iannone, A.F., Fetcho, R.N., Ferrer, M., Liston, C., Fishell, G., and De Marco García, N.V. (2018). Layer I Interneurons Sharpen Sensory Maps during Neonatal Development. Neuron *99*, 98–116.e7.

Chen, T.-W., Wardill, T.J., Sun, Y., Pulver, S.R., Renninger, S.L., Baohan, A., Schreiter, E.R., Kerr, R.A., Orger, M.B., Jayaraman, V., et al. (2013). Ultrasensitive fluorescent proteins for imaging neuronal activity. Nature *499*, 295–300.

Chen, N., Sugihara, H., and Sur, M. (2015). An acetylcholine-activated microcircuit drives temporal dynamics of cortical activity. Nat. Neurosci. *18*, 892–902.

Colonnese, M.T. (2014). Rapid developmental emergence of stable depolarization during wakefulness by inhibitory balancing of cortical network excitability. J. Neurosci. *34*, 5477–5485.

Colonnese, M.T., and Phillips, M.A. (2018). Thalamocortical function in developing sensory circuits. Curr. Opin. Neurobiol. *52*, 72–79.

Duan, Z.R.S., Che, A., Chu, P., Modol, L., Bollmann, Y., Babij, R., Fetcho, R.N., Otsuka, T., Fuccillo, M.V., Liston, C., et al. (2020). GABAergic restriction of network dynamics regulates interneuron survival in the developing cortex. Neuron *105*, 75–92.e5.

Feller, M.B. (1999). Spontaneous correlated activity in developing neural circuits. Neuron *22*, 653–656.

Flossmann, T., Kaas, T., Rahmati, V., Kiebel, S.J., Witte, O.W., Holthoff, K., and Kirmse, K. (2019). Somatostatin Interneurons Promote Neuronal Synchrony in the Neonatal Hippocampus. Cell Rep. *26*, 3173–3182.e5.

Golshani, P., Gonçalves, J.T., Khoshkhoo, S., Mostany, R., Smirnakis, S., and Portera-Cailliau, C. (2009). Internally mediated developmental desynchronization of neocortical network activity. J. Neurosci. *29*, 10890–10899.

González-Rueda, A., Pedrosa, V., Feord, R.C., Clopath, C., and Paulsen, O. (2018). Activity-Dependent Downscaling of Subthreshold Synaptic Inputs during Slow-Wave-Sleep-like Activity In Vivo. Neuron *97*, 1244–1252.e5.

Gribizis, A., Ge, X., Daigle, T.L., Ackman, J.B., Zeng, H., Lee, D., and Crair, M.C. (2019). Visual Cortex Gains Independence from Peripheral Drive before Eye Opening. Neuron *104*, 711–723.e3.

Guan, W., Cao, J.-W., Liu, L.-Y., Zhao, Z.-H., Fu, Y., and Yu, Y.-C. (2017). Eye opening differentially modulates inhibitory synaptic transmission in the developing visual cortex. eLife *6*, e32337199661.

Hanganu, I.L., Ben-Ari, Y., and Khazipov, R. (2006). Retinal waves trigger spindle bursts in the neonatal rat visual cortex. J. Neurosci. *26*, 6728–6736.

Harvey, A.R., Ehlert, E., Wit, J., Drummond, E.S., Pollett, M.A., Ruitenberg, M., Plant, G.W., Verhaagen, J., and Levelt, C.N. (2009). Use of GFP to Analyze Morphology, Connectivity, and Function of Cells in the Central Nervous System. In: Viral Applications of Green Fluorescent Protein (Hicks BW (Totowa, NJ: Humana Press), pp. 63–95.

Kato, H.K., Asinof, S.K., and Isaacson, J.S. (2017). Network-Level Control of Frequency Tuning in Auditory Cortex. Neuron *95*, 412–423.e4.

Katz, L.C., and Shatz, C.J. (1996). Synaptic activity and the construction of cortical circuits. Science *274*, 1133–1138.

Kepecs, A., and Fishell, G. (2014). Interneuron cell types are fit to function. Nature *505*, 318–326.

Kerschensteiner, D. (2014). Spontaneous Network Activity and Synaptic Development. Neuroscientist *20*, 272–290.

Kirkby, L.A., Sack, G.S., Firl, A., and Feller, M.B. (2013). A role for correlated spontaneous activity in the assembly of neural circuits. Neuron *80*, 1129–1144.

Kirmse, K., Kummer, M., Kovalchuk, Y., Witte, O.W., Garaschuk, O., and Holthoff, K. (2015). GABA depolarizes immature neurons and inhibits network activity in the neonatal neocortex in vivo. Nat. Commun. *6*, 7750.

Ko, H., Cossell, L., Baragli, C., Antolik, J., Clopath, C., Hofer, S.B., and Mrsic-Flogel, T.D. (2013). The emergence of functional microcircuits in visual cortex. Nature *496*, 96–100.

Krashes, M.J., Koda, S., Ye, C., Rogan, S.C., Adams, A.C., Cusher, D.S., Maratos-Flier, E., Roth, B.L., and Lowell, B.B. (2011). Rapid, reversible activation of AgRP neurons drives feeding behavior in mice. J. Clin. Invest. *121*, 1424–1428.

Kwon, H.-B., Kozorovitskiy, Y., Oh, W.-J., Peixoto, R.T., Akhtar, N., Saulnier, J.L., Gu, C., and Sabatini, B.L. (2012). Neuroligin-1-dependent competition regulates cortical synaptogenesis and synapse number. Nat Neurosci *15*, 1667–1674.

Leighton, A.H., and Lohmann, C. (2016). The Wiring of Developing Sensory Circuits-From Patterned Spontaneous Activity to Synaptic Plasticity Mechanisms. Front. Neural Circuits *10*, 71.

Luhmann, H.J., and Khazipov, R. (2018). Neuronal activity patterns in the developing barrel cortex. Neuroscience *368*, 256–267.

Maldonado, P.P., Nuno-Perez, A., Kirchner, J.H., Hammock, E., Gjorgjieva, J., and Lohmann, C. (2021). Oxytocin Shapes Spontaneous Activity Patterns in the Developing Visual Cortex by Activating Somatostatin Interneurons. Curr. Biol. *31*, 322–333.e5.

Markram, H., Toledo-Rodriguez, M., Wang, Y., Gupta, A., Silberberg, G., and Wu, C. (2004). Interneurons of the neocortical inhibitory system. Nat. Rev. Neurosci. *5*, 793–807.

Marques-Smith, A., Lyngholm, D., Kaufmann, A.-K., Stacey, J.A., Hoerder-Suabedissen, A., Becker, E.B.E., Wilson, M.C., Molnár, Z., and Butt, S.J.B. (2016). A Transient Translaminar GABAergic Interneuron Circuit Connects Thalamocortical Recipient Layers in Neonatal Somatosensory Cortex. Neuron *89*, 536–549.

Minlebaev, M., Ben-Ari, Y., and Khazipov, R. (2007). Network mechanisms of spindle-burst oscillations in the neonatal rat barrel cortex in vivo. J. Neurophysiol. *97*, 692–700.

Mòdol, L., Sousa, V.H., Malvache, A., Tressard, T., Baude, A., and Cossart, R. (2017). Spatial Embryonic Origin Delineates GABAergic Hub Neurons Driving Network Dynamics in the Developing Entorhinal Cortex. Cereb. Cortex *27*, 4649–4661.

Modol, L., Bollmann, Y., Tressard, T., Baude, A., Che, A., Duan, Z.R.S., Babij, R., De Marco García, N.V., and Cossart, R. (2020). Assemblies of perisomatic GABAergic neurons in the developing barrel cortex. Neuron *105*, 93–105.e4.

Montijn, J.S., Olcese, U., and Pennartz, C.M.A. (2016). Visual Stimulus Detection Correlates with the Consistency of Temporal Sequences within Stereotyped Events of V1 Neuronal Population Activity. J. Neurosci. *36*, 8624–8640.

Naskar, S., Narducci, R., Balzani, E., Cwetsch, A.W., Tucci, V., and Cancedda, L. (2019). The development of synaptic transmission is time-locked to early social behaviors in rats. Nat. Commun. *10*, 1195.

Pan, N.C., Fang, A., Shen, C., Sun, L., Wu, Q., and Wang, X. (2019). Early Excitatory Activity-Dependent Maturation of Somatostatin Interneurons in Cortical Layer 2/3 of Mice. Cereb. Cortex *29*, 4107–4118.

Pnevmatikakis, E.A., and Giovannucci, A. (2017). NoRMCorre: An online algorithm for piecewise rigid motion correction of calcium imaging data. J. Neurosci. Methods *291*, 83–94.

Pologruto, T.A., Sabatini, B.L., and Svoboda, K. (2003). ScanImage: flexible software for operating laser scanning microscopes. Biomed. Eng. Online *2*, 13.

R Core Team (2020). R (R Foundation for Statistical Computing).

Rahmati, V., Kirmse, K., Holthoff, K., Schwabe, L., and Kiebel, S.J. (2017). Developmental Emergence of Sparse Coding: A Dynamic Systems Approach. Sci. Rep. *7*, 13015.

Rochefort, N.L., Narushima, M., Grienberger, C., Marandi, N., Hill, D.N., and Konnerth, A. (2011). Development of direction selectivity in mouse cortical neurons. Neuron *71*, 425–432.

Rousseeuw, P.J. (1987). Silhouettes: A graphical aid to the interpretation and validation of cluster analysis. J. Comput. Appl. Math. *20*, 53–65.

Rueden, C.T., Schindelin, J., Hiner, M.C., DeZonia, B.E., Walter, A.E., Arena, E.T., and Eliceiri, K.W. (2017). ImageJ2: ImageJ for the next generation of scientific image data. BMC Bioinformatics *18*, 529.

Schindelin, J., Arganda-Carreras, I., Frise, E., Kaynig, V., Longair, M., Pietzsch, T., Preibisch, S., Rueden, C., Saalfeld, S., Schmid, B., et al. (2012). Fiji: an open-source platform for biological-image analysis. Nat. Methods *9*, 676–682.

Siegel, F., Heimel, J.A., Peters, J., and Lohmann, C. (2012). Peripheral and central inputs shape network dynamics in the developing visual cortex in vivo. Curr. Biol. *22*, 253–258.

Stefanelli, T., Bertollini, C., Lüscher, C., Muller, D., and Mendez, P. (2016). Hippocampal Somatostatin Interneurons Control the Size of Neuronal Memory Ensembles. Neuron *89*, 1074–1085.

Taniguchi, H., He, M., Wu, P., Kim, S., Paik, R., Sugino, K., Kvitsiani, D., Fu, Y., Lu, J., Lin, Y., et al. (2011). A resource of Cre driver lines for genetic targeting of GABAergic neurons in cerebral cortex. Neuron *71*, 995–1013.

Tononi, G., and Cirelli, C. (2006). Sleep function and synaptic homeostasis. Sleep Med. Rev. *10*, 49–62.

Torborg, C.L., and Feller, M.B. (2005). Spontaneous patterned retinal activity and the refinement of retinal projections. Prog. Neurobiol. *76*, 213–235.

Tremblay, R., Lee, S., and Rudy, B. (2016). GABAergic Interneurons in the Neocortex: From Cellular Properties to Circuits. Neuron *91*, 260–292.

Tuncdemir, S.N., Wamsley, B., Stam, F.J., Osakada, F., Goulding, M., Callaway, E.M., Rudy, B., and Fishell, G. (2016). Early Somatostatin Interneuron Connectivity Mediates the Maturation of Deep Layer Cortical Circuits. Neuron *89*, 521–535.

Urban-Ciecko, J., and Barth, A.L. (2016). Somatostatin-expressing neurons in cortical networks. Nat. Rev. Neurosci. *17*, 401–409.

Valeeva, G., Tressard, T., Mukhtarov, M., Baude, A., and Khazipov, R. (2016). An Optogenetic Approach for Investigation of Excitatory and Inhibitory Network GABA Actions in Mice Expressing Channelrhodopsin-2 in GABAergic Neurons. J. Neurosci. *36*, 5961–5973.

van Versendaal, D., and Levelt, C.N. (2016). Inhibitory interneurons in visual cortical plasticity. Cell. Mol. Life Sci. *73*, 3677–3691.

Verhaagen, J., Hobo, B., Ehlert, E.M.E., Eggers, R., Korecka, J.A., Hoyng, S.A., Attwell, C.L., Harvey, A.R., and Mason, M.R.J. (2018). Small Scale Production of Recombinant Adeno-Associated Viral Vectors for Gene Delivery to the Nervous System. Methods Mol. Biol. *1715*, 3–17.

Ward, J.H. (1963). Hierarchical Grouping to Optimize an Objective Function. J. Am. Stat. Assoc. *58*, 236–244.

Winnubst, J., Cheyne, J.E., Niculescu, D., and Lohmann, C. (2015). Spontaneous activity drives local synaptic plasticity in vivo. Neuron *87*, 399–410.

Wosniack, M.E., Kirchner, J.H., Chao, L.-Y., Zabouri, N., Lohmann, C., and Gjorgjieva, J. (2021). Adaptation of spontaneous activity in the developing visual cortex. eLife *10*, e61619.

Xu, H.P., Furman, M., Mineur, Y.S., Chen, H., King, S.L., Zenisek, D., Zhou, Z.J., Butts, D.A., Tian, N., Picciotto, M.R., and Crair, M.C. (2011). An instructive role for patterned spontaneous retinal activity in mouse visual map development. Neuron *70*, 1115–1127.

Xu, H.-P., Burbridge, T.J., Chen, M.-G., Ge, X., Zhang, Y., Zhou, Z.J., and Crair, M.C. (2015). Spatial pattern of spontaneous retinal waves instructs retinotopic map refinement more than activity frequency. Dev. Neurobiol. *75*, 621–640.

Zhang, J., Ackman, J.B., Xu, H.P., and Crair, M.C. (2011). Visual map development depends on the temporal pattern of binocular activity in mice. Nat. Neurosci. *15*, 298–307.

STAR★METHODS

KEY RESOURCES TABLE

REAGENT or RESOURCE	SOURCE	IDENTIFIER
Antibodies		
Chicken anti Vglut2	SynapticSystems	Synaptic Systems Cat# 135 404; RRID:AB_887884
Rat anti SST	Millipore	Millipore Cat# MAB354; RRID:AB_2255365
Bacterial and virus strains		
AAV1-hSyn-DIO-hM4D(Gi)-mCherry	Bryan Roth (Krashes et al., 2011, Addgene plasmid # 44362).	Addgene plasmid # 44362
pAAV-Syn-GCaMP6s-WPRE-SV40	Addgene plasmid, (Chen et al., 2013) packaged in-house	Addgene plasmid # 100843
Chemicals, peptides, and recombinant proteins		
Picrotoxin	Sigma-Aldrich	SID 24278188
Clozapine	Tocris	PubChem ID 2818
Deposited data		
DS1, Excitatory and inhibitory inputs during spontaneous activity	This paper	10.6084/m9.figshare.14336594
DS2, Spontaneous activity before and after DREADD suppression: two-photon	This paper	10.6084/m9.figshare.14334011
DS3, Spontaneous activity before and after DREADD suppression: epifluorescence	This paper	10.6084/m9.figshare.14330156
Experimental models: Organisms/strains		
Mouse: C57BL/6J	Janvier Labs	N/A 25/03/2014 aangepaard met BL/6JOlaHsd
Mouse: CBA	Harlan Laboratories	N/A
Mouse: Rosa26.tdTomato	The Jackson Laboratory	Ai14D, JAX 7908
Mouse: SST-IRES-cre	The Jackson Laboratory; Taniguchi et al., 2011	JAX: 13044
Oligonucleotides		
Primer for WPRE: 5′-CCCACTT GGCAGTACATCAA-3′	Eurogentec	N/A
Primer for WPRE: 5′-GGAAAGTC CCATAAGGTCATGT-3′	Eurogentec	N/A
Recombinant DNA		
Plasmid: GCaMP6s, cloned into pCAGGS	Douglas Kim; Chen et al., 2013	Addgene plasmid # 40753
Plasmid: DsRed, cloned into pCAGGS	Christiaan Levelt	N/A
Software and algorithms		
Software: MATLAB	MathWorks	https://www.mathworks.com/
Software: R	R Core Team, 2020	https://www.R-project.org/
Software: R lme4 package	Bates et al., 2014	https://cran.r-project.org/web/packages/lme4/lme4.pdf
Analysis pipeline for simultaneous two-photon imaging and whole-cell voltage-clamp recording: custom	This paper	https://github.com/ahleighton/calcium_with_ephys
Analysis pipeline for SST suppression: custom	This paper	https://github.com/ahleighton/sst_dreadd_analysis

(*Continued on next page*)

Continued

REAGENT or RESOURCE	SOURCE	IDENTIFIER
Analysis preprocessing pipeline: preprocessing Calcium imaging	Flatiron Institute, Simons Foundation	https://github.com/flatironinstitute/NoRMCorre
Analysis pre-processing pipeline: custom	Winnubst et al., 2015	N/A
ImageJ2 (Fiji)	Rueden et al., 2017; Schindelin et al., 2012	https://imagej.net/software/fiji
Clampfit	Molecular Devices	https://www.moleculardevices.com/
Igor	WaveMetrics, Inc	https://www.wavemetrics.com/

RESOURCE AVAILABILITY

Lead contact

Further information and requests for resources, data, code, and reagents should be directed to and will be fulfilled by the lead contact, Christian Lohmann (c.lohmann@nin.knaw.nl).

Materials availability

This study did not generate new unique reagents.

Data and code availability

Dataset DS1, Excitatory and inhibitory inputs during spontaneous activity, is available at https://dx.doi.org/10.6084/m9.figshare.14336594. Dataset DS2, Spontaneous activity before and after DREADD suppression: two-photon is available at https://figshare.com/articles/dataset/Two_Photon_SST-GiDREADD/14334011 and DS3, Spontaneous activity before and after DREADD suppression: epifluorescence, at https://figshare.com/articles/dataset/Epifluorescence_Imaging_with_SST-GiDREADD/14330156. Unprocessed data are available upon reasonable request.

The analysis pipeline for simultaneous two-photon imaging and whole-cell voltage-clamp recording is available at https://github.com/ahleighton/calcium_with_ephys. The analysis pipeline used for quantifying the effect of SST DREADD suppression is available at https://github.com/ahleighton/sst_dreadd_analysis.

EXPERIMENTAL MODEL AND SUBJECT DETAILS

All experimental procedures were approved by the institutional animal care and use committee of the Royal Netherlands Academy of Sciences.

Organism

Neonatal mice of both sexes were used. All pups were aged between postnatal days (P) 8-14 and weight between 5 and 10 g. Pups were housed in shared nests (two dams) with a maximum of 10 pups per cage. Animals were drug naive. At the time of data collection, animals had previously undergone either viral injection at P0/P1 or in utero electroporation as embryos and subsequent toe-clipping for identification purposes, to achieve expression of the calcium sensor. Where the calcium sensor was acutely injected, animals had undergone no previous procedures. Where control animals were used, littermates were randomly assigned to experimental groups.

Genotypes

Wild-type mice were either C57BL/6J mice or C57BL/6J x CBA F1 mice. These mice open their eyes at P14. SST-IRES- cre (JAX 13044) mice were designed by Dr. Z. Josh Huang and ordered from Jackson Labs (SST-IRES-Cre; Taniguchi et al., 2011). To produce labeled SST interneurons, this line was crossed with a tdTomato-reporter mice (Ai14D, JAX 7908).

These mice were maintained on a mixed C57BL/6J x 129S background.

METHOD DETAILS

Surgeries

In utero electroporation

For wide-field calcium imaging shown in Figures 1 and S4, pyramidal neurons in layer 2/3 of the visual cortex were transfected with GCaMP6s (2 mg/ml) and DsRed (2 mg/ml) at E16.5 using in utero electroporation (Harvey et al., 2009). Pregnant mice were anesthetized with isoflurane and a small incision (1.5–2 cm) was made in the abdominal wall. The uterine horns were carefully removed from the abdomen, and DNA was injected into the lateral ventricle of embryos using a sharp glass electrode. Voltage pulses (five square

wave pulses, 30 V, 50-ms duration, 950-ms interval, custom-built electroporator) were delivered across the brain with tweezer electrodes covered in conductive gel. Embryos were rinsed with warm saline solution and returned to the abdomen, after which time the muscle and skin were sutured.

Virus injection

Pups (P0-P1) were anaesthetized using hypothermia (induced for 6 minutes). A small cut was made in the skin before insertion of a glass pipette and injection of 27 nL of virus in V1 (two-photon imaging) or 27 nL in V1 and a second injection of 27 nL in RL (to achieve greater spread, for wide-field imaging). Animals were injected with a mix of 1:1 AAV1-hSyn-DIO-hM4D(Gi)-mCherry and pAAV-Syn-GCaMP6s-WPRE-SV40 or a mixture of 1:1 PBS and pAAV-Syn-GCaMP6s-WPRE-SV40. pAAV-hSyn-DIO-hM4D(Gi)-mCherry was a gift from Bryan Roth (Krashes et al., 2011, Addgene plasmid # 44362).

Craniectomy for acute imaging

Animals were anesthetized with isoflurane (3% in 1 l/min O_2). After anesthesia had become effective, lidocaine was used for local analgesia and a head bar with an opening (Ø 4 mm) above the visual cortex (0.5–2.5 mm rostral from lambda and 1–3 mm lateral from the midline) was attached to the skull with superglue and dental cement. For calcium imaging, a small craniectomy above the visual cortex was performed. The exposed cortical surface was kept moist with cortex buffer (125 mM NaCl, 5 mM KCl, 10 mM glucose, 10 mM HEPES, 2 mM $MgSO_4$ and 2 mM $CaCl_2$ [pH 7.4]).

For recordings performed under anesthesia (used during whole-cell recordings in Figures 1 and 4, and wide-field recordings in Figure 1), isoflurane levels were lowered to 0.7%–1%. Prior to awake imaging (Datasets in Figures 2, 3, and S1–S3), the animals were given 60 minutes to recover from anesthesia.

Virus production

AAV vectors were produced as described previously (Verhaagen et al., 2018). In short, AAV1 serotype helper plasmid and pAAV-hSyn-DIO-hM4D(Gi)-mCherry or pAAV-Syn-GCaMP6s were co-transfected into HEK293T cells. Seventy-two hours later, the cells were harvested, lysed and centrifuged. Subsequently the viral particles were purified from the supernatant using an iodixanol density gradient and further concentrated using an Amicon Ultra-15 centrifugal filter. Titers were determined by quantitative PCR for the WPRE element in the viral genomes (vg). Primers for WPRE: 5′-CCCACTTGGCAGTACATCAA-3′ and 5′-GGAAAGTCCCATAAGGTC ATGT-3′. Titers were 2E+12 vg/ml for pAAV-hSyn-DIO-hM4D(Gi)-mCherry and pAAV-Syn-GCAMP6s.

Calcium imaging methods

Calcium sensors

Figures 1A–1G, 4, and S3: The calcium-sensitive dye Oregon Green 488 BAPTA-1 AM (OGB-1, Invitrogen) was dissolved in 4 μL pluronic F-127, 20% solution in DMSO (Invitrogen) and further diluted (1: 10) in dye buffer (150 mM NaCl, 2.5 mM KCl, and 10 mM HEPES) to yield a final concentration of 1 mM. The dye was then pressure-ejected at 10–12 psi for 12–13 min with a micropipette (3–5 MΩ) attached to a picospritzer (Toohey).

Figures 1H–1N, 2, 3, S1, S2, and S4: Animals were injected (see: virus injection) with a mix of 1:1 AAV1-hSyn-DIO-hM4D(Gi)-mCherry and pAAV-Syn-GCaMP6s-WPRE-SV40 or (control animals) a mixture of 1:1 PBS and pAAV-Syn-GCaMP6s-WPRE-SV40.

Image acquisition

Two-photon

In vivo calcium imaging was performed on either a Nikon (A1R-MP) with a 0.8/16x water-immersion objective and a Ti:Sapphire laser (Chameleon II, Coherent) or a Movable Objective Microscope (Sutter Instruments) with a Ti:Sapphire laser (MaiTai HP, Spectra Physics) and a 0.8/40x water-immersion objective (Olympus) using Nikon or ScanImage software (Pologruto et al., 2003). Scan mirror positions were recorded to synchronize calcium imaging and electrophysiology. Images of 330 by 330 μm were recorded at 5-10 Hz.

Epifluorescence

Epifluorescence was recorded at 20 Hz using custom-built LabVIEW software (National Instruments) using a digital CCD camera (QImaging), a 0.16/4x (Olympus) objective and a xenon-arc lamp (Sutter Instrument Company). To map the cortical surface and identify the location of V1, we labeled primary sensory areas post hoc by immunohistochemistry for the thalamocortical axon marker vGlut2 (Figure S4).

Dreadd activation

Animals expressing the above virus were first imaged at baseline. The fast DREADD agonist clozapine was then injected subcutaneously at 0.5 mg/kg. We expected to see effects in a relatively narrow time window and restricted our analyses to 30 minutes post-injection. In fact, we observed that clozapine administration caused a decrease in amplitude, relative to baseline, in 3 out of 4 imaged SST cells during that period.

Electrophysiology acquisition

In vivo: Current clamp

Membrane potential was recorded in current clamp at 10 kHz and filtered at 3 kHz (Multiclamp 700b; Molecular Devices). For current clamp recordings electrodes (4.5–6 MΩ) were filled with intracellular solution (105 mM K gluconate, 10 mM HEPES, 30 mM KCl, 10 mM phosphocreatine, 4 mM MgATP, and 0.3 mM GTP; Golshani et al., 2009). 10 μM Alexa 594 hydrazide (Invitrogen) was added to allow targeted whole-cell recordings. The mean network participation based on calcium imaging was 45% (L-events)

and 94% (H-events). The patched cell participated (fired at least 1 action potential) in 70% of L-events and 100% of H-events. Taking a threshold of three action potentials or more gives participation rates similar to the calcium imaging (41% and 94%), implying that we can pick up cells that fire three action potentials or more.

In vivo: Voltage clamp

Synaptic currents were recorded in voltage clamp at 10 kHz and filtered at 3 kHz (Multiclamp 700b; Molecular Devices). For voltage clamp recordings, electrodes were filled with intracellular solution (120 mM $CsMeSO_3$, 8 mM NaCl, 15 mM $CsCl_2$, 10 mM TEA-Cl, 10 mM HEPES, 5 mM QX-314, 4 mM MgATP, 0.3 mM Na-GTP; Kwon et al., 2012).

The reversal potential for chloride was −28 mV and the reversal potential for excitatory currents was 0 mV, corrected for the measured liquid junction potential. The reversal potential for both excitatory and inhibitory inputs were checked empirically throughout each recording (by observing the direction of currents at a range of potentials) and found to correspond to the expected values. During whole-cell recording we alternated between measurements of inhibitory and excitatory current (5 minutes of each before switching) so that changes in patch quality over time would affect each condition equally.

In vitro: Current-clamp

Acute 300 μm coronal slices of the visual cortex were dissected. Pups were sacrificed by decapitation and their brains were immersed in ice-cold cutting solution (in mM): 2.5 KCl, 1.25 NaH_2PO_4, 26 $NaHCO_3$, 20 Glucose, 215 Sucrose, 1 $CaCl_2$, 7 $MgCl_2$ (Sigma), pH 7.3-7.4, bubbled with 95%/5% O_2/CO_2. Slices were obtained with a vibratome (VT1200 S, Leica) and subsequently incubated at 34°C in artificial cerebrospinal fluid (ACSF, in mM): 125 NaCl, 3.5 KCl, 1.25 NaH_2PO_4, 26 $NaHCO_3$, 20 Glucose, 2 $CaCl_2$, 1 MgCl2 (Sigma), pH 7.3-7.4. After 45 minutes, slices were transferred to the electrophysiology setup, kept at room temperature and bubbled with 95%/5% O_2/CO_2. For patch recordings, slices were transferred to a recording chamber and perfused (3 ml/min) with ACSF solution bubbled with 95%/5% O_2/CO_2 at 34°C.

Layer 2/3 SST^+ or SST^- cells were identified using a fluorescence/IR-DIC video microscope (Olympus BX51WI). SST^+ interneurons were identified by the mCherrry protein fluorescence from mice injected with pAAV-hSyn-DIO-hM4D(Gi)-mCherry. Current-clamp recordings were made with a MultiClamp 700B amplifier (Molecular Devices), filtered with a low pass Bessel filter at 10 kHz and digitized at 20-50 kHz (Digidata 1440A, Molecular Devices). Series resistance was assessed during recordings and neurons showing a series resistance > 30 MΩ or change > 30% were discarded. Digitized data were analyzed offline using Clampfit 10 (Molecular Devices) and Igor (WaveMetrics).

Electrodes were filled with an intracellular solution containing (in mM): 122 KGluconate, 10 HEPES, 13 KCl, 10 phosphocreatine disodium salt hydrate, 4 ATP magnesium salt, 0.3 GTP sodium salt hydrate (Sigma), pH 7.3. Clozapine 10 μM (Tocris) was bath applied. After breaking the seal, variable current injection was applied to keep cells at −60 mV. To test the excitability of the cells, current injection from −80 pA to 160 pA was applied in 10 pA increments.

QUANTIFICATION AND STATISTICAL ANALYSIS

Image processing

Two-photon

As described previously (Maldonado et al., 2021), two-photon image processing drift and movement artifacts were removed from each recording using NoRMCorre (Pnevmatikakis and Giovannucci, 2017). Delta F stacks were made using the mean fluorescence per pixel as baseline. ROIs were hand-drawn using the Fiji distribution of ImageJ2 (Rueden et al., 2017; Schindelin et al., 2012). Automated transient detection and further data processing was performed using custom-made MATLAB software (MathWorks).

Epifluorescence

Delta F stacks were made using the average fluorescence per pixel as baseline. V1 was identified based on activity coordinates and shape, after this method of identification was confirmed through immunohistochemistry for vGluT2 (Figure S4).

Signal detection

Two-photon

In two-photon recordings (Figures 1C–1F, 3, 4, S2, and S3), activations within each cell were detected as in Siegel et al. (2012) as a peak with both an absolute height and relative prominence of at least 5% $\Delta F/F_0$. When more than 20% of the total number of cells in the field of view were active simultaneously, the activation was considered an event.

Epifluorescence

In epifluorescence imaging (Figures 1G–1L, 2D–2O, and S1), events were detected as calcium peaks with an amplitude above 2x the standard deviation of the signal. Connected component analysis was used to determine whether simultaneously occurring events were distinct, or part of one spreading activation. The total distance traveled by an event was measured by calculating the x and y coordinates of the center of mass of activation in each frame, and summing the difference between these coordinates for each successive frame. Speed was determined as this distance, divided by the number of seconds during which this event was detected (event duration). Analysis was restricted to events that activated at least one pixel in V1.

Electrophysiology

Electrophysiology measurements were aligned to images using custom-built MATLAB software. When an event was detected in calcium imaging, the corresponding electrophysiology trace was extracted from 8 s before and after the calcium peak. Contamination

from events happening close together in time was removed by automatic detection and manual confirmation. Charge transferred during an excitatory or inhibitory input burst was measured as the area under the curve of the detected burst.

Receiver-operation characteristic curves and random forest classification were analyzed in MATLAB. A separate classifier was built for excitatory and inhibitory inputs for each recorded animal, using every event detected in that condition in that animal. Each run built 100 bagged classification trees. Out-of-bag prediction to classify events; i.e., for each event to be classified, only the trees in which that event was not featured was used to predict whether, based on the electrophysiology, the event was an L- or H-event. The success of this classification was then quantified by comparing it against whether the event was an L- or H-event, based on the participation as measured with calcium imaging, using the 80% cut-off to define an H-event. Success of out-of-bag prediction was used to compare the inhibitory and excitatory models. One animal was excluded from random forest classification due to insufficient inhibitory events to allow for good out-of-bag predictions.

Hierarchical clustering and silhouette analysis was performed in MATLAB. As described in Montijn et al., (2016), we used Ward's method (Ward, 1963) hierarchical clustering to construct dendrograms of all events. Clustering was based on the number of action potentials fired and duration (Figure 1F) or the amplitude and activated area (when performed on wide-field data). Hierarchical clustering was performed within each animal. Silhouette curves were made based on the dendrogram (Rousseeuw, 1987), where a single datapoint in a cluster was given a silhouette value of 0. The optimal number of clusters was taken as the overall maximum.

Statistical tests

The test used, n, and the definition of n for each test can be found in the figure legends. Where one paired measurement from each animal was used, we performed paired two-tailed t tests.

In Figure 2B, each paired value represents a cell before and after application of clozapine. Input-output curves for the *in vitro* clozapine experiments were generated by calculating the cell firing rate at each current injection step in control and clozapine conditions.

In Figures 2H–2M, we additionally fit a multi-level model on all recorded events, that took the nested nature of this data into account (Aarts et al., 2014) and allowed us to test the interaction of the injected viral construct (either containing hMDi-DREADD or control) with the presence or absence of clozapine. We fitted a linear mixed-effects model using the lme4 package (Bates et al., 2014) in R (R Core Team, 2020) with baseline versus clozapine and DREADD versus control mice as fixed effects, with random intercepts and slopes for the metric that was being evaluated. To determine whether there was an interaction effect between the clozapine administration and the mouse line, we fitted a full model which included the interaction and a reduced model which did not. Whether there was a significant interaction was determined by comparing the full model with the reduced model using an ANOVA. Results of paired t tests in Figure 2 are only shown where this ANOVA indicated a significant contribution of the interaction term. Similarly, in Figures 3D and 3E we performed a two-way ANOVA to confirm that the effects we detected were also significant relative to control animals.

In Figure S3, we used the non-parametric two-sample Kolmogorov-Smirnov tests to compare distributions of amplitude and participation in both SST expressing and non-SST expressing cells.